

Supporting Information

HF-free Synthesis of Si/C Yolk/Shell Anodes for Lithium-ion Batteries

*Xingkang Huang, Xiaoyu Sui, Hannah Yang, Ren Ren, Yingpeng Wu, Xiaoru Guo, and Junhong Chen**

Experimental

Synthesis. First, 200 mg Si nanoparticles were dispersed in 20 mL deionized (DI) water, containing 1 M oxalic acid and 0.2 mL hydrogen peroxide solution (30 wt. %). After stirring for 2 h, the Si nanoparticles were separated using centrifugation and washed twice with DI water, followed by two rounds of rinsing using ethanol ($\geq 99.5\%$, Sigma-Aldrich). The resulting hydroxyl-group-enhanced Si was dispersed in 20 mL ethanol, and 0.1 mL methacryloxy(propyl)trimethoxysilane (MPS) in 10 mL ethanol was added dropwise while stirring. After the addition of the MPS solution, the dispersion was kept stirring for 72 h, then was centrifuged at 12,000 rpm for 10 min and washed with ethanol four times. The resulting MPS-modified Si was dispersed in 20 mL ethanol using sonication. Then, 5 mL of the MPS-modified Si/ethanol solution was transferred into a 100 mL three-neck, round-bottom flask, followed by the addition of 20/10 mL ethanol/DI water, 0.1 g Polyvinylpyrrolidone (PVP), 0.06 mg azobis[2-(2-imidazolin-2-yl) propane] dihydrochloride (AIBI), and 1.5 mL styrene. After purging N_2 for 30 min, the flask was sealed to allow the reaction to proceed for 18 h. The obtained precipitate was washed with DI water and isopropanol; due to their different densities the Si-free particles (white) were separated from the PS-coated Si (Si@PS, yellow) using centrifugation. The Si@PS was then sulfonated overnight using concentrated sulfuric acid, and then washed and centrifuged. The sulfonated Si@PS was dispersed in 100 mL DI water with 2 mL concentrated sulfuric acid and 0.49 g ammonium persulfate at 2 °C, into which 0.2 mL aniline was added dropwise with pump at a flow rate of approximately $0.5 \mu\text{L min}^{-1}$. The solution was maintained

at 2 °C for approximately 18 h to allow the polyaniline to uniformly coat on the PS surface. The as-obtained Si@PS@PAni was washed completely with DI water and isopropanol, and calcined at 300 °C for 30 min and then at 650 °C for 1 h. The PAni layer was converted to C shell while the PS was removed, leaving a very thin layer of C on Si surface due to the very low carbon yield of the PS, thereby forming Si@C@void@C, a yolk/shell material.

Characterization. The morphology of the as-prepared samples was characterized by scanning electron microscopy (SEM) and energy-dispersive X-ray spectroscopy (EDS), performed on a Hitachi S-4800 equipped with a Bruker EDS detector, and transmission electron microscopy (TEM), carried out on a Hitachi H-9000-NAR operating at an acceleration voltage of 300 kV. Powder X-ray diffraction (XRD) was performed on a Bruker D8 DISCOVER diffractometer with Cu K α radiation. Raman spectroscopy was carried out using a Renishaw 1000B Raman microscope with a 632.8-nm HeNe laser with three accumulations of 10 s each. The surface area and pore size measurements were carried out by Brunauer, Emmett, and Teller (BET) N₂ adsorption/desorption on a Micromeritics ASAP 2020. Thermogravimetric/differential thermal analysis (TG/DTA) was carried out under air flow (100 mL min⁻¹) at a heating rate of 10 °C min⁻¹ on a SDT 2660 Simultaneous DSC-TGA instrument. X-ray photoelectron spectroscopy (XPS) spectra of samples were obtained using an HP5950A ESCA spectrometer with monochromatic Al K α radiation as the X-ray source. Fourier transform infrared (FTIR) spectroscopy was measured on a Nicolet 5700 FT-IR spectrometer in the range of wave numbers 400–4000 cm⁻¹ at a resolution 4 cm⁻¹. The electrical conductivity of the as-prepared material was calculated by measuring the impedance of the powders with various pressures, in which the powders were pressed into a diameter of 12.7 mm with a thickness of ~300 microns. The tap density of the Si@C@void@C was measured according to the standard test method for determination of tap density of metallic powders and compounds (ASTM B527–06), where we used a 1-mL measuring pipette instead of a 25-mL graduated glass cylinder because of the limited sample amount.

Preparation of Electrodes and Coin Cells. The charge/discharge performance was characterized by using 2032-type coin cells that were assembled in an argon-filled glove box, with oxygen and moisture content below 1 ppm. Electrodes were prepared by mixing the as-prepared Si@C@void@C as the active material, sodium carboxymethyl cellulose, poly(acrylic acid), and carbon black as a conductor with a weight ratio of 80:5:5:10 to form a slurry. The resulting slurries were coated onto a Cu foil (12- μm in thickness) current collector using the doctor blade method. After drying and pressing, the Cu foil was cut into disks (1.1 cm in diameter) with typical electrode material loadings of ca. 1 mg cm^{-2} . Then, 1 M LiPF_6 dissolved in ethylene carbonate/ethyl methyl carbonate (40:60, v/v) with additives of fluoroethylene carbonate (5 wt. %) and vinylene carbonate (1 wt. %) was employed as an electrolyte.

Electrochemistry. The coin cells were tested on a LAND battery tester with a cut-off voltage range between 0.1 and 2.5 V. Note that the lithiation behavior was defined as “charge” because the Si@C@void@C is an anode material for LIBs (Kasavajjula, U.; Wang, C. S.; Appleby, A. J. Nano- and bulk-silicon-based insertion anodes for lithium-ion secondary cells. *J. Power Sources* 2007, 163, 1003-1039). Cyclic voltammetry (CV) of the as-prepared anode was measured on a PARSTAT 4000 electrochemical station using a three-electrode cell, with the Si@C@void@C electrode as the working electrode, a lithium disk as the counter electrode, and a lithium ring as the reference electrode. CV was carried out at a scanning rate of 0.05 mV s^{-1} . Electrochemical impedance spectroscopy (EIS) was tested between 10,000-0.1 Hz with an amplitude of 10 mV.

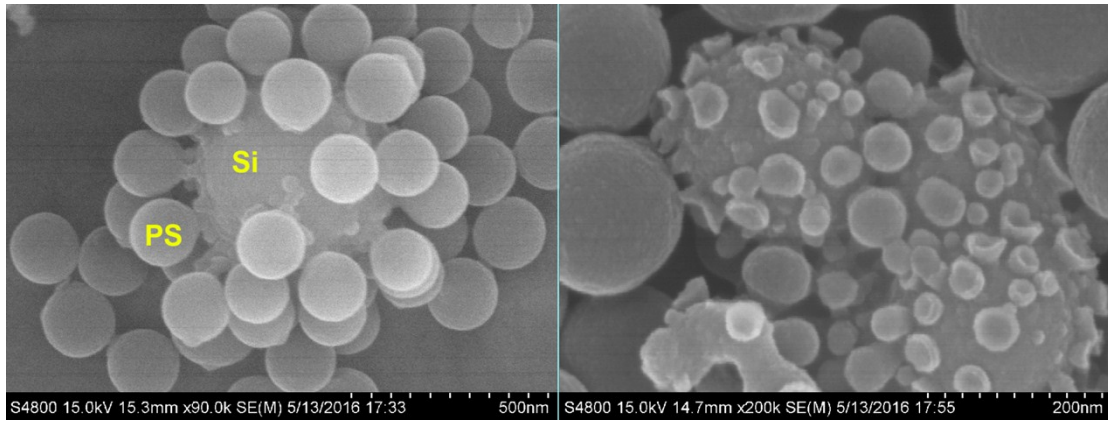


Figure S1. SEM images of an unsuccessful coating of PS onto Si without enhancing the OH groups on the Si surface; instead, PS was attached by the means of particles. With the rich OH groups, the PS was able to uniformly coat onto the Si surface. The figure on the right shows the PS “trail” on the Si surface as evidence of detachment of PS particles.

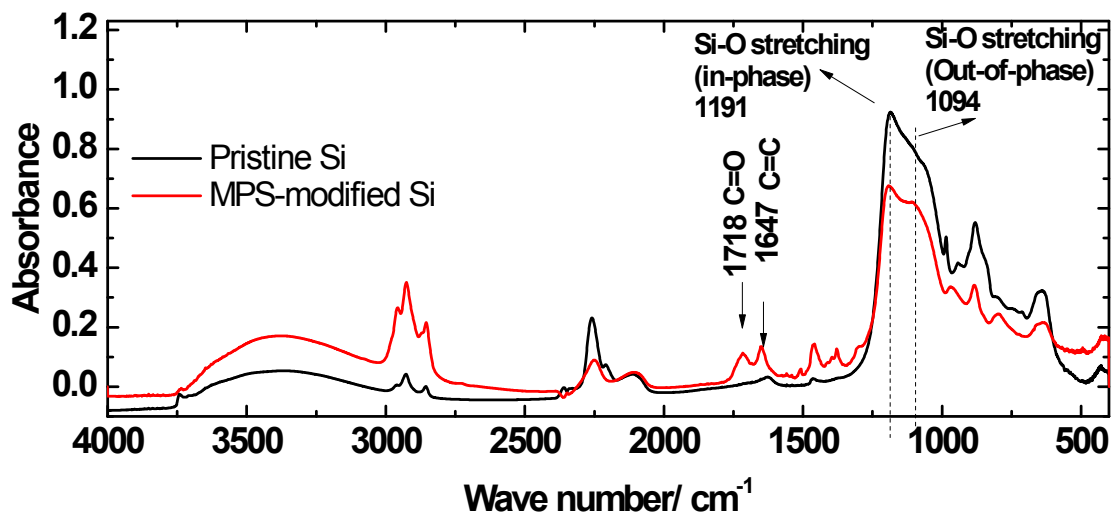


Figure S2. FT-IR spectra of pristine Si and MPS-modified Si. The bands at ~ 1718 and 1647 cm^{-1} are associated to the stretching vibrations of C=O and C=C groups, respectively, indicating the successful grafting MPS onto Si surface.

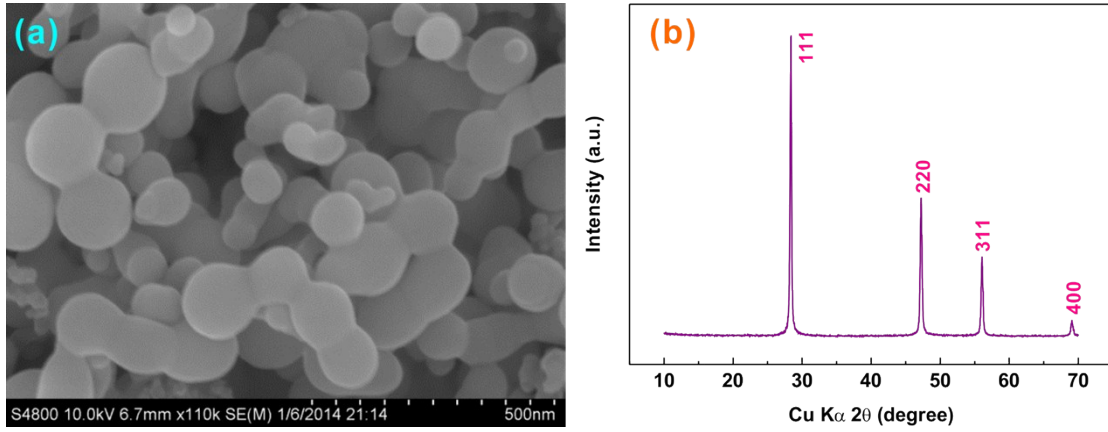


Figure S3. (a) SEM image and (b) XRD pattern of pristine Si nanoparticles. The sharp and narrow XRD peaks suggest the well-crystallized Si particles.

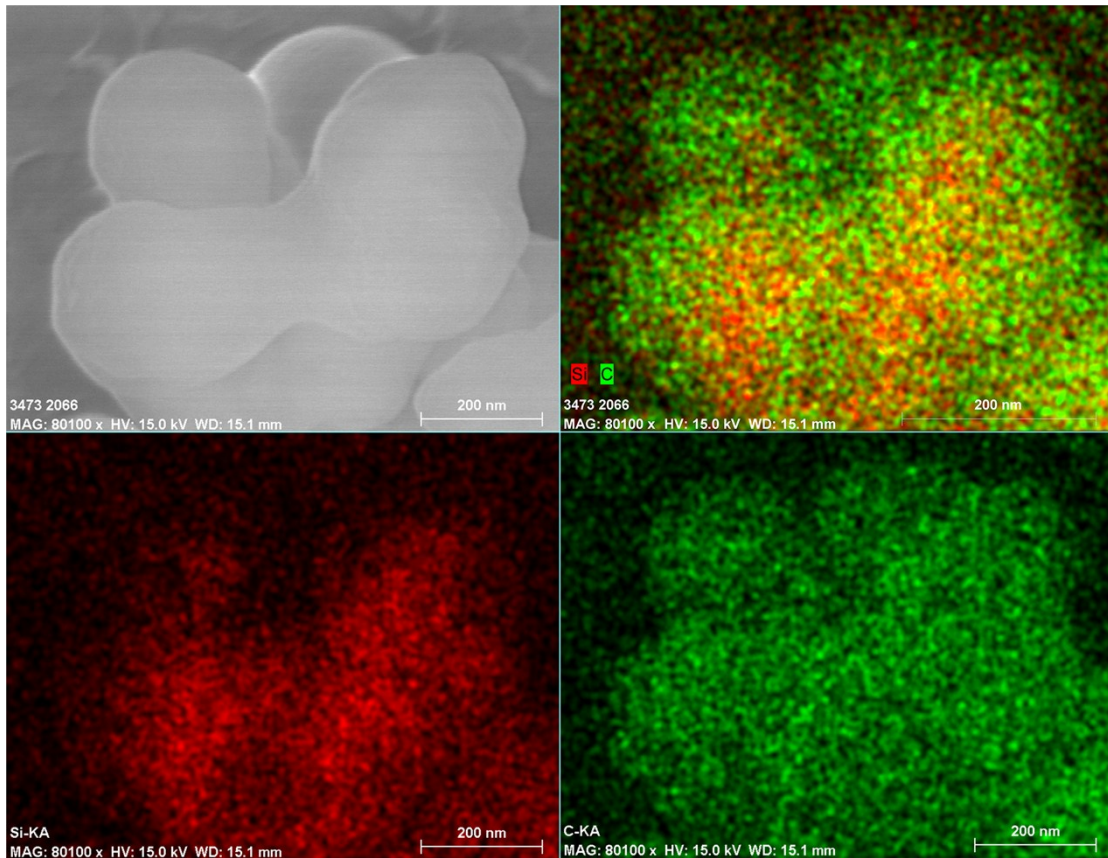


Figure S4. SEM image of Si@PS and its corresponding EDS elemental mapping.

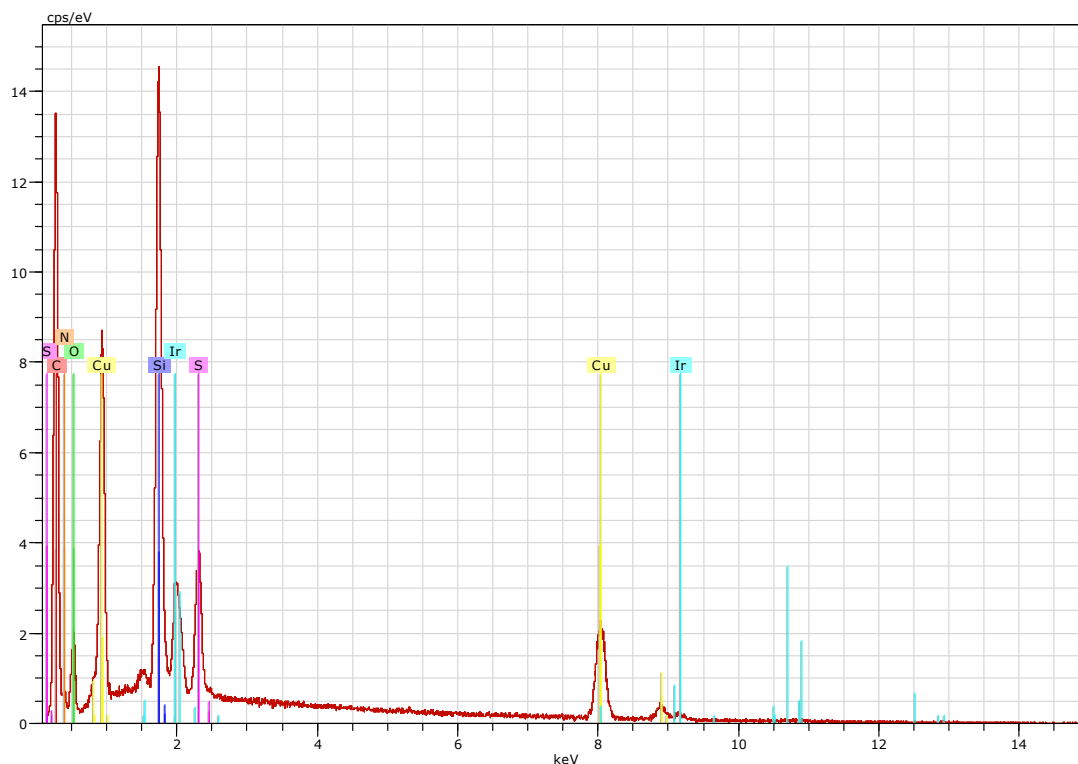


Figure S5. EDS analysis of Si@PS@PAni. The analysis was conducted on a Cu tape, in which Ir was used to enhance the electrical conductivity. The results are summarized in Table S1.

Table S1. EDS analysis results of Si@PS@PAni.

El	AN	Series	unn. C [wt.%]	norm. C [wt.%]	Atom. C [at.%]	Error [%]
C	6	K-series	20.61	23.09	46.15	2.5
N	7	K-series	7.75	8.69	14.88	1.5
O	8	K-series	6.08	6.82	10.23	1.0
Si	14	K-series	11.79	13.20	11.28	0.5
S	16	K-series	3.33	3.73	2.79	0.1
Cu	29	K-series	32.19	36.06	13.62	2.1
Ir	77	M-series	7.50	8.41	1.05	0.3
Total:			89.26	100.00	100.00	

The contents of C, N, O, Si, and S were calculated to be 41.58, 15.65, 12.28, 23.77, and 6.72 wt. %, respectively, by excluding the Cu and Ir.

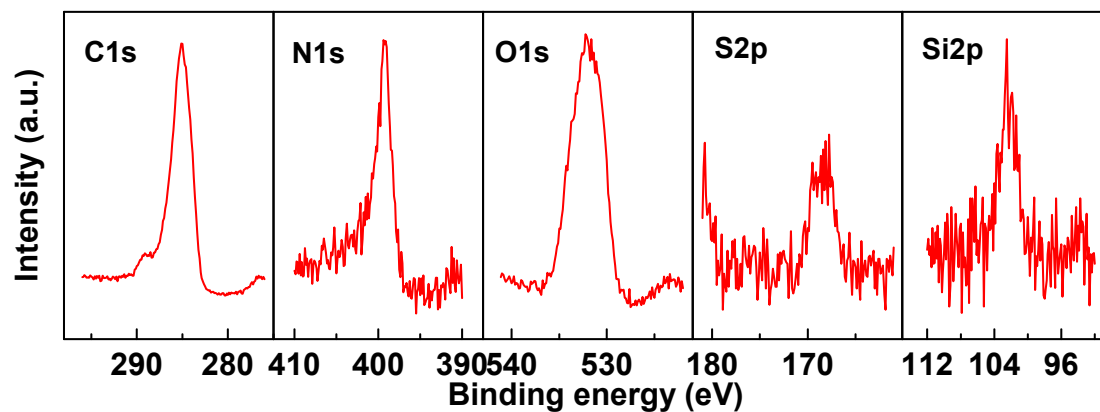


Figure S6. XPS analysis of Si@PS@PAni.

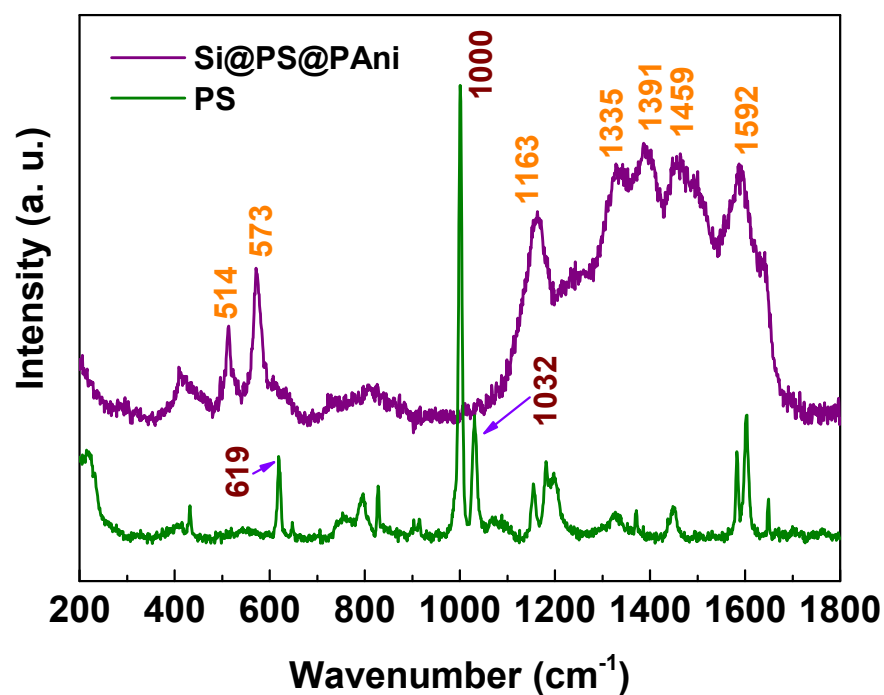


Figure S7. Raman spectra of PS and Si@PS@PAni. The laser was reduced to 10% in case the polymers were destroyed by the heat from the laser. Calibration was done according to the Si wafer (519.5 cm⁻¹) before running the test. After coating PAni, Raman spectroscopy was unable to detect the PS, suggesting a very good coating of the PAni on the PS.

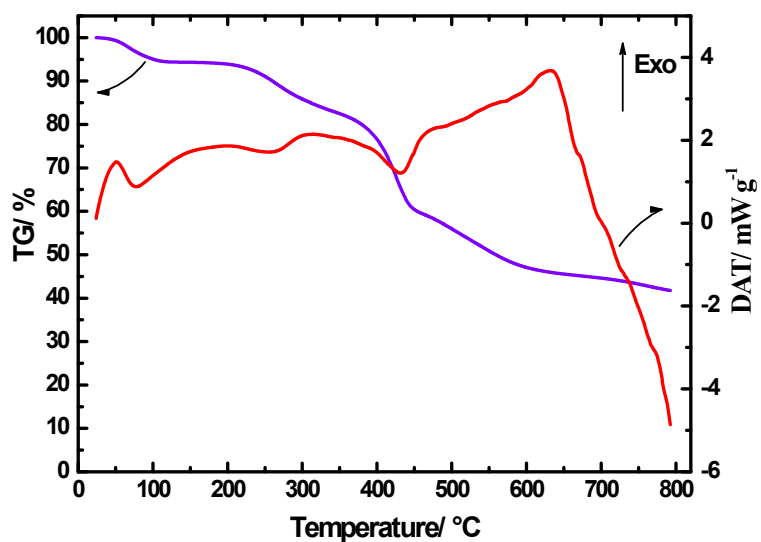


Figure S8. TG/DTA of PS@PAni.

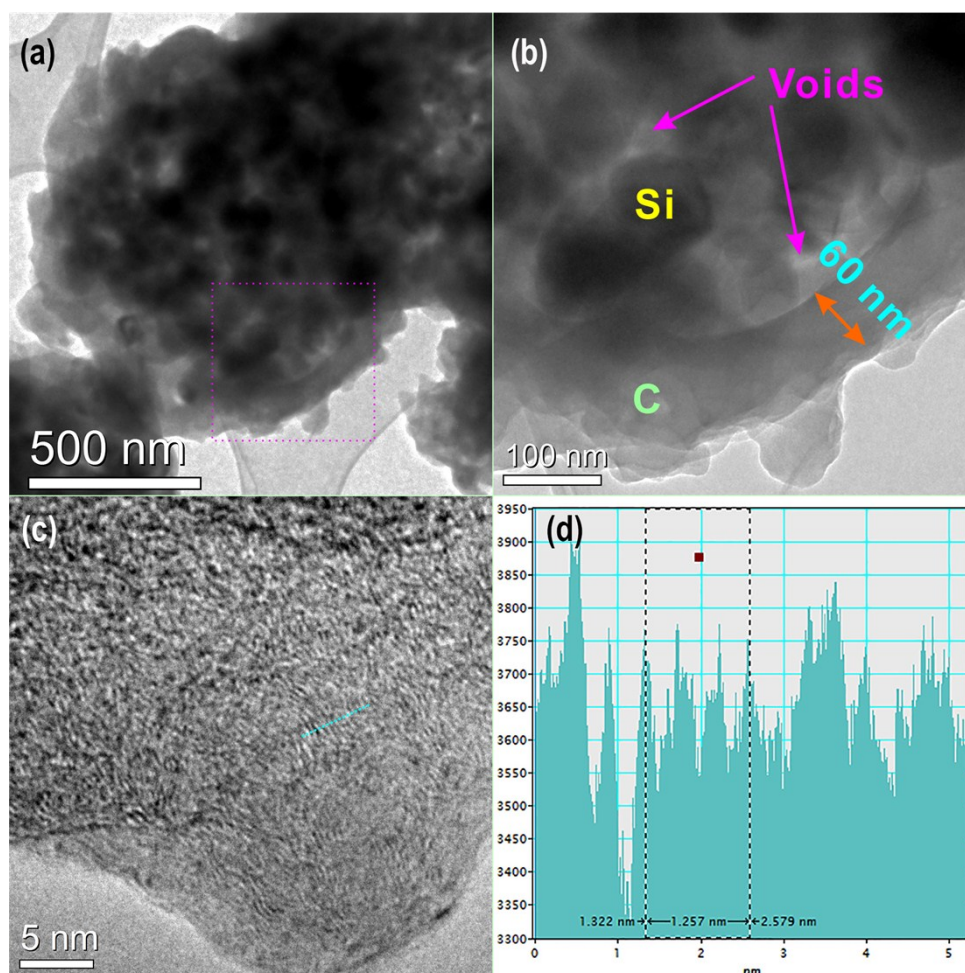


Figure S9. (a-b) TEM images, HRTEM image, and profile analysis in the marked zone in (c) for the Si@C@void@C. Multiple Si nanoparticles were encapsulated in a 1.2- μm C shell. The thickness of the C shell is approximately 60 nm. Si particles and

voids also can be seen clearly in (a) and (b). Only local lattice fringes were observed; the lack of long-range order suggests the poor crystallinity of the C shell. The profile analysis of the marked zone in (c) indicates the d-spacing of the C is approximately 0.42 nm, higher than that of typical graphite (0.335 nm for plane 002). This is due to the broadening effect of nanocrystallites.

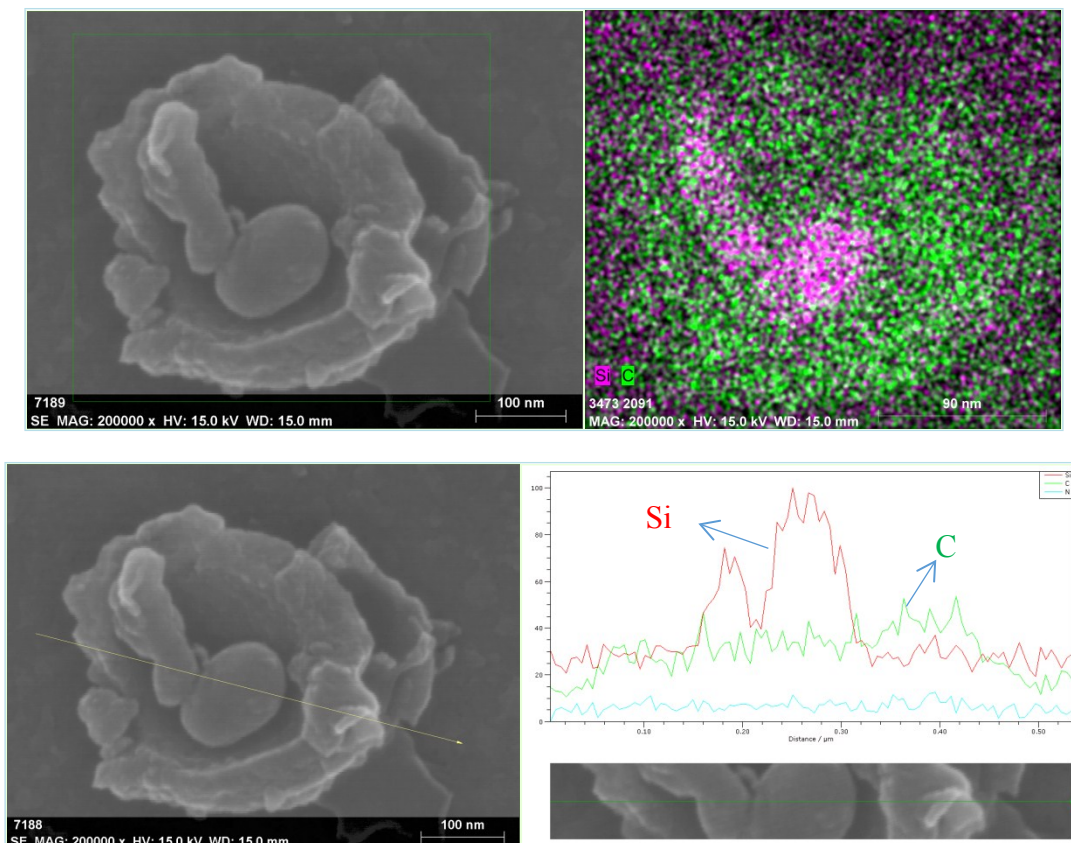


Figure S10. EDS elemental mapping (upper) and line scan (lower) analysis of a broken Si@C@void@C particle, indicating the Si yolk sitting in the hollow C shell.

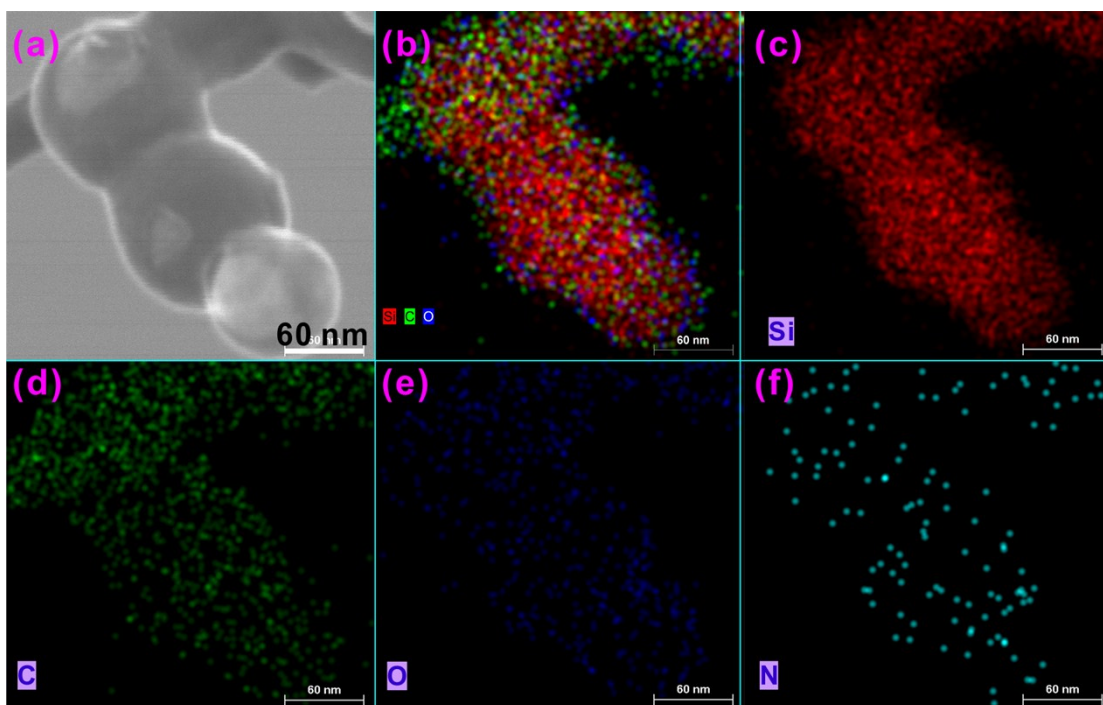


Figure S11. (a) SEM image of Si nanoparticles escaping from broken exterior C shell and (b-f) the corresponding EDS elemental mapping analysis. The thin layer of C was observed coating on the Si nanoparticles; N was barely detected in this layer of C (the randomly distributed bright blue dots in (f) indicate more like noise than N signal), which is due to this layer of C resulted from the decomposition of PS. The sample was held on a Lacey carbon film on 300 mesh copper grid.

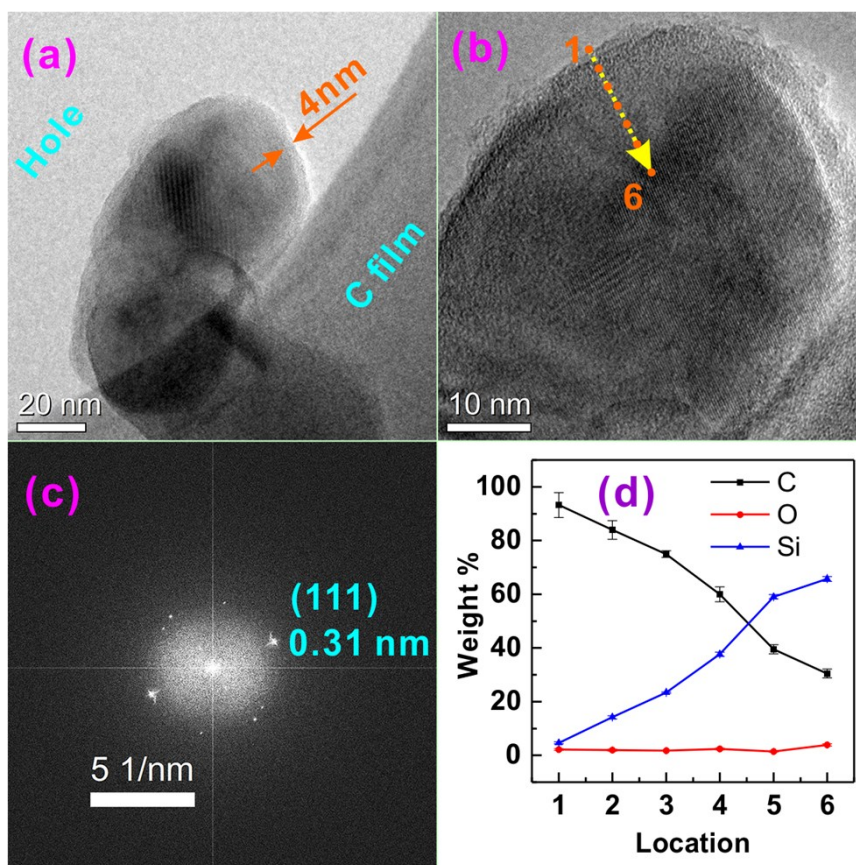


Figure S12. (a, b) TEM images of the Si nanoparticles escaping from broken exterior C shell, (c) fast Fourier transform (FFT) image resulted from (b), and (d) EDS analysis for C, O, and Si, in which six positions were analyzed as marked in (b). the decreasing C content and increasing Si from the surface toward the bulk indicate the the thin layer of C on the Si surfaces. The thickness of the C coat is approximately 2-4 nm as in (b). The FFT image shows the d -spacing of 0.31 nm, which originated from the (111) plane of Si. Note that the sample was held on a Lacey carbon film on 300 mesh copper grid.

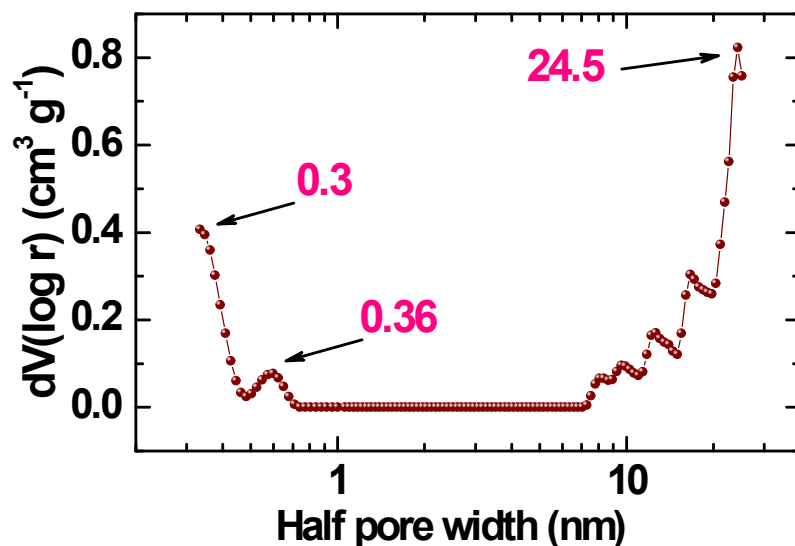


Figure S13. Pore size analysis based on a quenched solid density functional theory (QSDFT) kernel applied to the adsorption branch using a cylindrical/spherical pore model, showing the micropores with pore sizes of 1.12 nm and smaller than 0.6 nm. Note that the QSDFT results exhibit the majority pore sizes distributed at approximately 45 nm; however, the QSDFT method offers reliable results of micropores while the BJH approach provides more accurate pore sizes for mesopores.

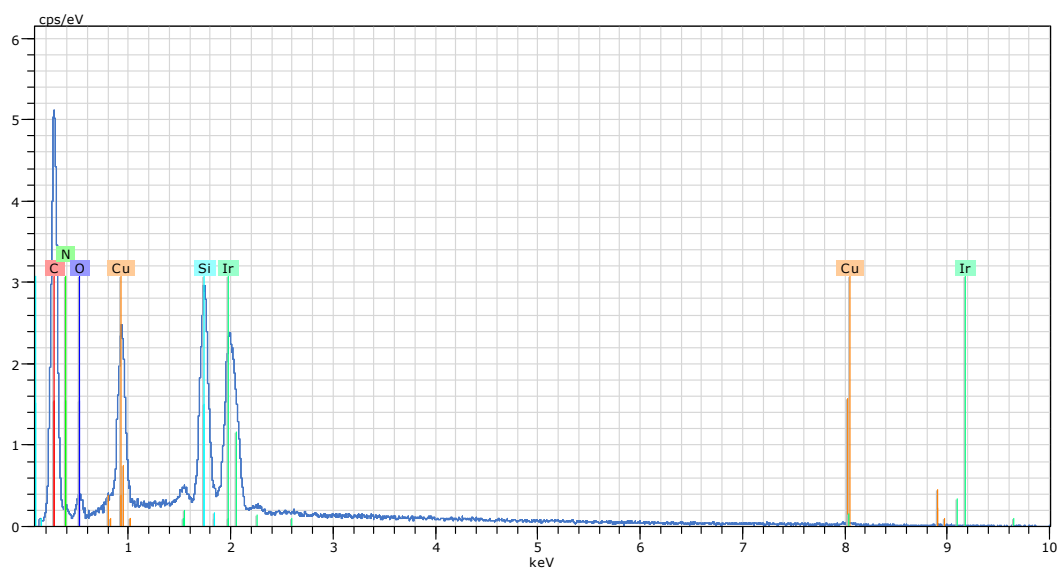


Figure S14. EDS analysis of Si@C@void@C. The results are summarized in Table S2.

Table S2. The EDS analysis results.

El	AN	Series	unn. C [wt.%]	norm. C [wt.%]	Atom. C [at.%]	Error [%]
C	6	K-series	43.98	44.01	65.22	5.6
N	7	K-series	12.16	12.17	15.46	2.9
O	8	K-series	3.87	3.88	4.31	0.9
Si	14	K-series	17.17	17.18	10.89	0.7
Cu	29	L-series	10.70	10.71	3.00	1.9
Ir	77	M-series	12.05	12.06	1.12	0.5
Total:			99.94	100.00	100.00	

The C, N, O, and Si contents in the Si@C@void@C were calculated to be 56.98, 15.76, 5.02, 22.24 w.t %, respectively, when excluding Cu and Ir.

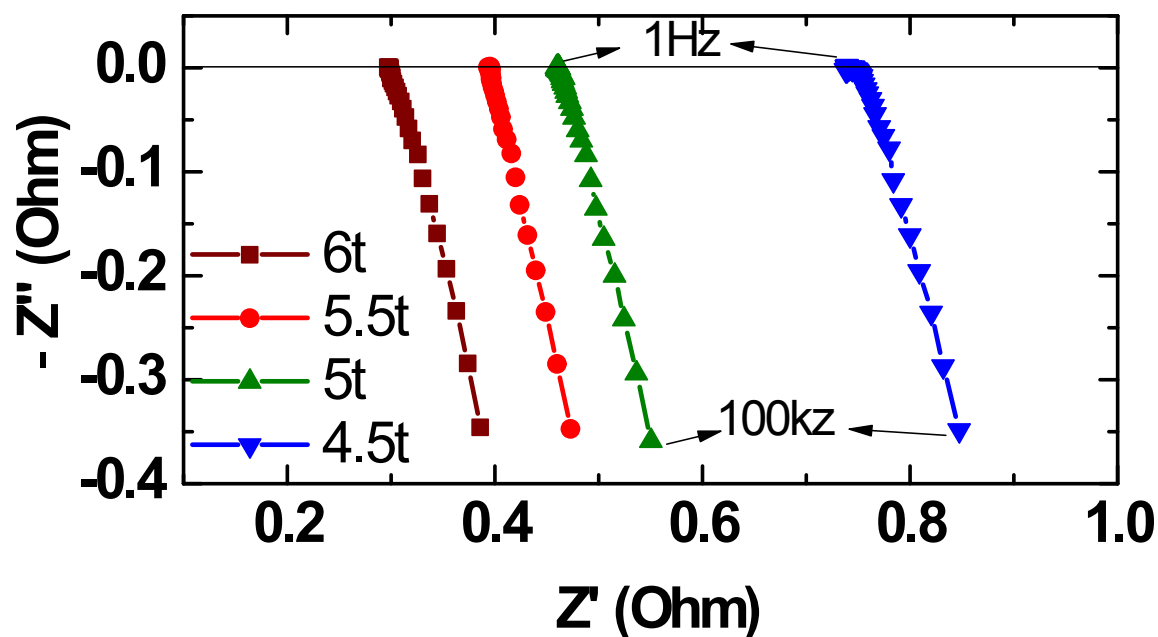


Figure S15. Nyquist plots of the powders of the as-prepared Si@C@void@C. The powders were pressed into ~300 microns with a diameter of 12.7 mm.

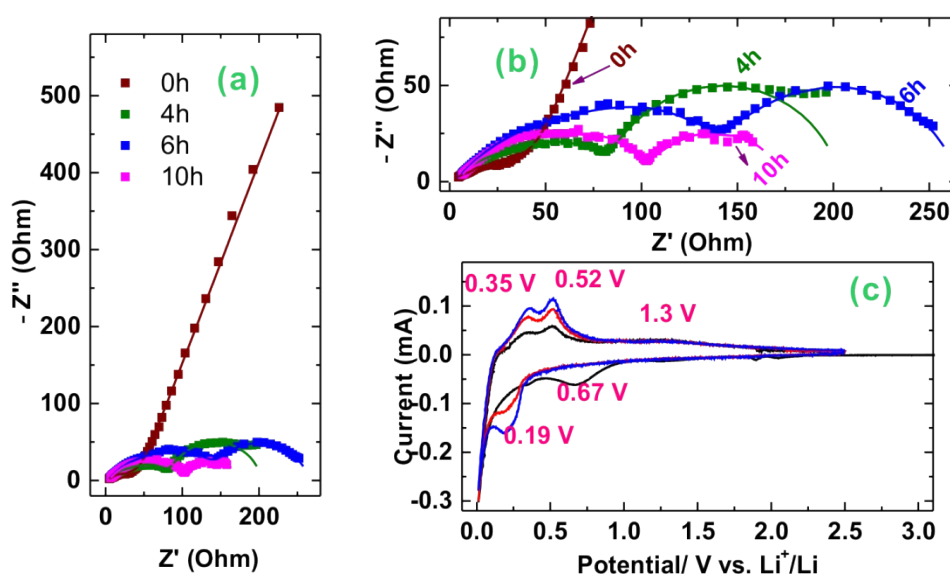


Figure S16. (a, b) EIS performance, and (c) CV behaviors, in which the cathodic peaks at 0.67 and 0.19 V are related to the formation of SEI layer while the anodic peaks at 0.35 and 0.52 V are associated with delithiation of Si; the peak at 1.3 V is due to the delithiation from poorly crystallized C. The scattered points in the Nyquist plots are experimental results; the solid lines are fitting/simulation results, in which

the scales of real and image parts are equally displayed to avoid twisting the semicircles.

Because the Si@C@void@C depicted a moderate rate capability, we conducted the electrochemical impedance spectroscopy (EIS) test to determine the reason. Similar to other Si anodes (*Adv. Mater.* 2014, 26, 4326-32; *RSC Adv.* 2015, 5, 38660-38664), the impedance of Si@C@void@C changed along with the states of charge (Figure S16a,b). At the fully discharged state, the Nyquist plot of the Si@C@void@C anode apparently consisted of a semicircle and an inclined line; however, two peaks were observed at the high-frequency zone in the Bode plot (Figure S17c), suggesting two time constants related to the SEI layer and the charge transfer process, respectively. Unlike C-free Si anodes without charge transfer resistance at the fully discharged state (*Adv. Mater.* 2014, 26, 4326-32; *RSC Adv.* 2015, 5, 38660-38664; *ACS Appl. Mat. Interfaces* 2013, 5, 11965-11970), the Si@C@void@C anode possessed a finite charge transfer resistance because the poorly crystallized C was still active at a voltage higher than 2 V, as indicated by the charge/discharge curves in Figure 4b.

When the Si@C@void@C anode was charged for various amounts of time at 80 mA g⁻¹, the inclined line at the low-frequency zone disappeared while developing two apparent semicircles (Figure S16). By analyzing the Bode plots of the Si@C@void@C anode at the charged states, we identified three semicircles instead. Taking the state of charge at 4 h as an example, the peak at the high-frequency zone in the Bode plot is asymmetric, which was fitted to two peaks (Figure S18). All the EIS results were fitted using the equivalent circuits shown in Figure S19 and summarized in Table S3. The relatively large impedance is consistent with the moderate rate performance of the Si@C@void@C.

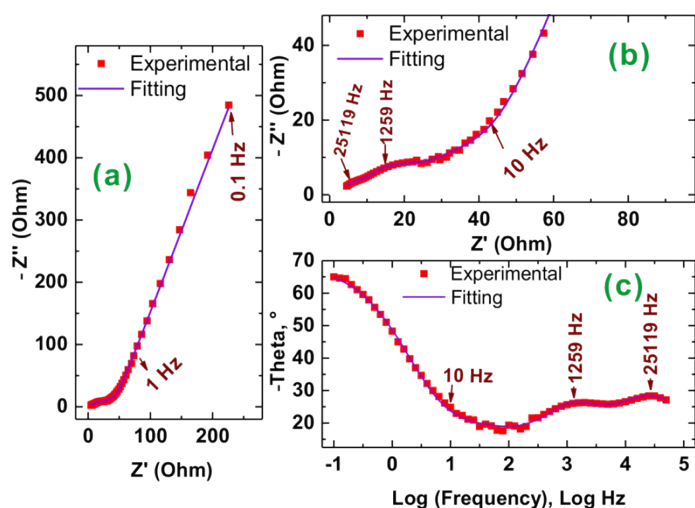


Figure S17. (a,b) Nyquist plots and (c) Bode plot of the Si@C@void@C anode when fully discharged to 2.5 V. Note that a few data points (typically two to three) at the highest frequency zone were deleted; otherwise, the fitting error would increase remarkably. At very high frequencies, the signals are prone to interference by noise.

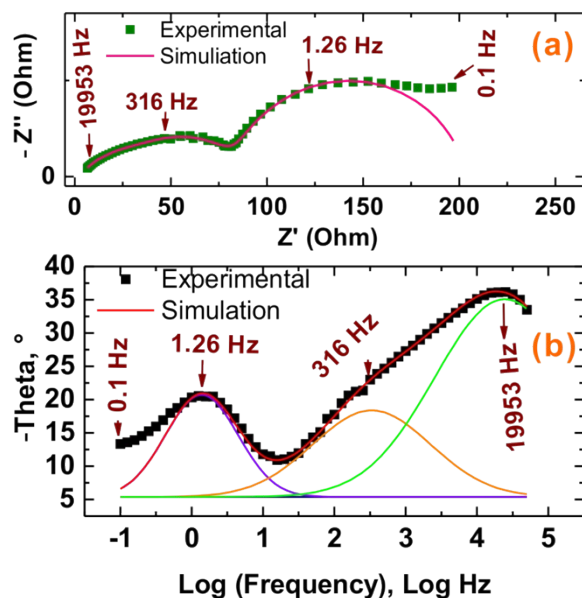


Figure S18. (a) Nyquist plot and (b) Bode plot of the Si@voide@C anode after charging 4 h at 100 mA g⁻¹. Apparently, there are two semicircles in the Nyquist plot; however, the asymmetric peak at the high-frequency zone in the Bode plot indicates an additional semicircle in the Nyquist. Peak fitting suggests three peaks at 19,953, 326, and 1.26 Hz, respectively; therefore, a three time-constant equivalent circuit should be applied to fit the EIS result. Note also that at a low frequency the impedance was significantly affected by the diffusion resistance, which makes the

fitting very challenging. From the Bode plot, we can see that the diffusion resistance did not show any effect on the impedance at frequencies higher than 1.26 Hz; therefore, we set the fitting zone using 1.26 Hz as the lower limit. After fitting the experimental impedance at the selected zone, we simulated the impedance for all the data points by extending the lower frequency limit to 0.1 Hz. In this way, although the simulation plot deviates from the experimental data at the low-frequency zone, the fitting results are accurate.

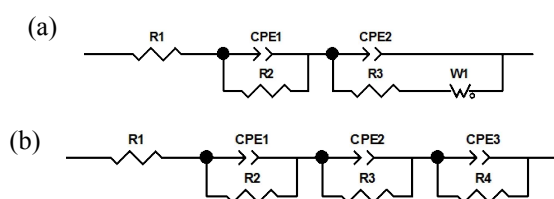


Figure S19. Equivalent circuits with (a) two time constants and (b) three time constants for fitting the EIS results.

Table S3. EIS fitting results for the Si@C@void@C anode at various states of charge.

State of charge	Voltage/ V	R1/ Ω	R1 Err. / Ω	R2/ Ω	R2 Err. / Ω	R3/ Ω	R3 Err. / Ω	R4 / Ω	R4 Err. / Ω	W1-R / Ω	W1-R Err. / Ω
Fully discharged	2.032	2.66	0.22	10.2	1.53	6.42	1.70	N/A	N/A	69.97	1.73
4h charged	0.245	2.64	0.22	43.28	5.03	35.37	5.43	135.6	5.62	N/A	N/A
6h charged	0.168	3.34	0.09	108.7	9.21	33.01	8.78	120.8	4.25	N/A	N/A
Fully charged	0.050	3.87	0.12	97.96	3.18	4.53	2.11	68.65	3.03	N/A	N/A

The EIS was tested after the CV scan (0.05 mV s⁻¹) for three cycles, which is equivalent to the activation process for the Si@C@void@C electrode. The electrode was charged at 80 mA g⁻¹ for various durations to reach various states of charge. The EIS was measured after resting for 3 h at the open circuit potential at each state of charge. R1, R2, R3, R4, and W1-R represent Ohmic, SEI layer, charge transfer (on the C), charge transfer (on the Si), and Li⁺ diffusion resistances, respectively. The fitting errors for the resistances are relatively high, which could be due to the complication of the yolk/shell structure. In addition, the very close time constants between R2 and R3 made them difficult to separate, which could increase the fitting errors.

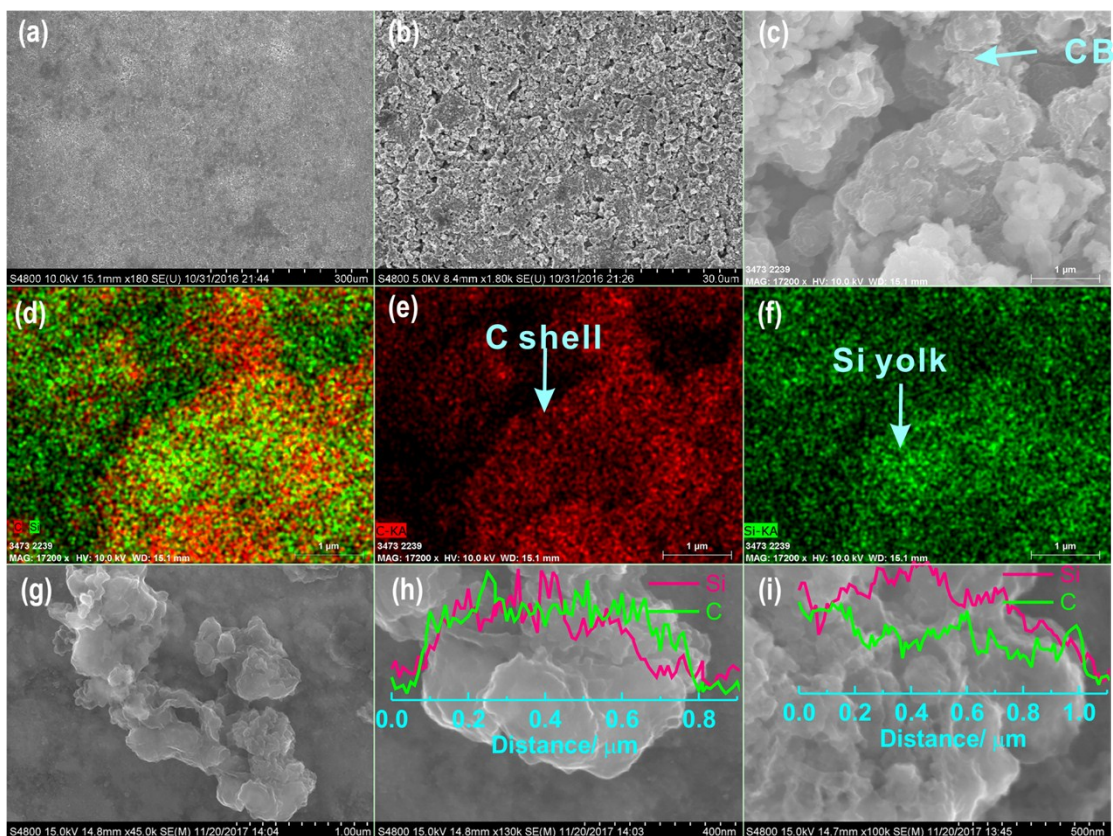


Figure S20. (a-c) SEM images of Si@C@void@C electrode after 500 cycles at 1,000 mA g⁻¹, in which no large crack was observed on the entire electrode, (d-f) EDS elemental mapping corresponding with the SEM image in (c), and (g-i) SEM images of Si@C@void@C particles and their corresponding EDS line scan analyses, in which the particles were collected from the electrode after 500 cycles, washed by dimethyl carbonate, acetone, and 1 vol.% HCl solution in sequence to eliminate the interference of the SEI layers. Carbon black (CB), C shell, and Si yolk are marked by arrows.

Table S4. Comparison of performance of yolk/shell Si/C materials for lithium-ion batteries.

Materials	Capacity retention for 100 cycles	Long-term cycling performance	HF involved	Ref.
mpSi@Void@mpC	67% of 790 mAh/g at 200 mA/g	N/A	Yes	[1]
Si@SiO ₂ @C@HF	86% of 762 mA h/g at 1A/g	59% for 300 cycles at 1A/g	Yes	[2]
Si@HC_3	69% of 1625 mAh/g at 200 mA/g	N/A	Yes	[3]
Si/void/SiO ₂ /void/C	84% of 1147 mAh/g at 460 mA/g	83% for 430 cycles at 460 mA/g; 80% for 1000 cycles at 4.8A/g	Yes	[4]
Si@void@C	78% of 2820 mAh/g at C/50 (for 50 cycles)	88%, 81%, and 74% for 500, 750, and 1000 cycles, respectively at 1C rate	Yes	[5]
Si@C@void@C	78% of 1750 mAh/g at 500 mA/g (for 50 cycles)	Not available	Yes.	[6]
Si@void@C	Not available	78.6% for 400 cycles at 420 mA/g.	Yes	[7]
Si@void@C	84.8% of ~1150 mAh/g at C/10	Not available	Yes	[8]
Si@double-shelled carbon	57.2% of 1698.6 mAh/g at 50 mA/g	Not available	Yes	[9]
Si@void@C pomegranate	Not available	87.7% for 1000 cycles	Yes	[10]
p-Si NRs@void@NC	Not available	93.6% for 300 cycle at 0.5A/g	No	[11]
Si@void@C	77.8% of ~1082 mAh/g at 1A/g (50 cycles)	Not available	No	[12]
Si@C@void@C	91% of 710 mAh/g at 200 mA/g	100% for 500 cycles at 1A/g	No	This work

Note: The capacity retention was calculated based the maximum capacity instead of initial one during cycling.

Reference:

- [1] Y. C. Ru, D. G. Evans, H. Zhu, W. S. Yang, RSC Adv. 2014, 4, 71.
- [2] X. L. Li, P. Meduri, X. L. Chen, W. Qi, M. H. Engelhard, W. Xu, F. Ding, J. Xiao, W. Wang, C. M. Wang, J. G. Zhang, J. Liu, J. Mater. Chem. 2012, 22, 11014.
- [3] S. R. Chen, M. L. Gordin, R. Yi, G. Howlett, H. Sohn, D. H. Wang, PCCP 2012, 14, 12741.
- [4] L. Y. Yang, H. Z. Li, J. Liu, Z. Q. Sun, S. S. Tang, M. Lei, Sci Rep-Uk 2015, 5.
- [5] N. Liu, H. Wu, M. T. McDowell, Y. Yao, C. M. Wang, Y. Cui, Nano Lett. 2012, 12, 3315.
- [6] J. Xie, L. Tong, L. W. Su, Y. W. Xu, L. B. Wang, Y. H. Wang, J. Power Sources 2017, 342, 529.
- [7] J. P. Yang, Y. X. Wang, S. L. Chou, R. Y. Zhang, Y. F. Xu, J. W. Fan, W. X. Zhang, H. K. Liu, D. Y. Zhao, S. X. Dou, Nano Energy 2015, 18, 133.

- [8] X. C. Xiao, W. D. Zhou, Y. N. Kim, I. Ryu, M. Gu, C. M. Wang, G. Liu, Z. Y. Liu, H. J. Gao, *Adv. Funct. Mater.* 2015, 25, 1426.
- [9] Z. Sun, S. Y. Tao, X. F. Song, P. Zhang, L. Gao, *J. Electrochem. Soc.* 2015, 162, A1530.
- [10] N. Liu, Z. D. Lu, J. Zhao, M. T. McDowell, H. W. Lee, W. T. Zhao, Y. Cui, *Nat. Nanotechnol.* 2014, 9, 187.
- [11] F. H. Du, Y. Z. Ni, Y. Wang, D. Wang, Q. Ge, S. Chen, H. Y. Yang, *ACS Nano* 2017, 11, 8628.
- [12] L. Pan, H. B. Wang, D. C. Gao, S. Y. Chen, L. Tan, L. Li, *Chem. Commun.* 2014, 50, 5878.

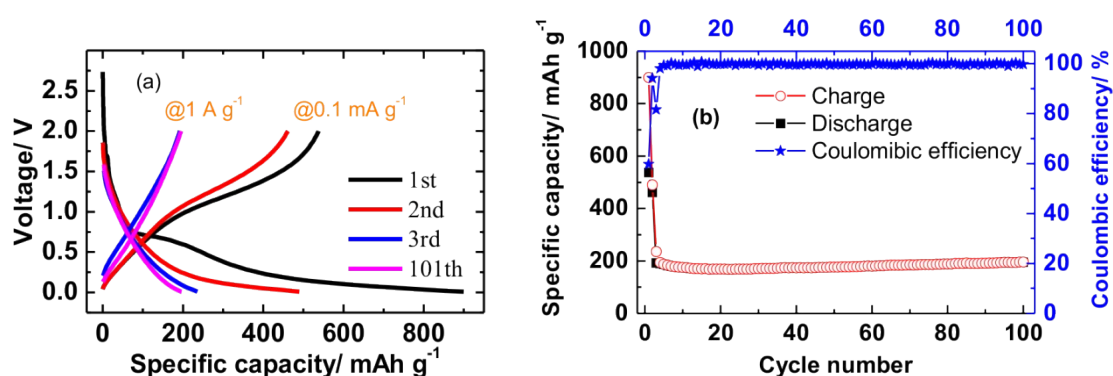


Figure S21. (a) Charge/discharge curves and (b) cyclic performance of a hollow C, prepared using PANi-coated PS (PS@PAni) in the absence of Si. The cell was activated at 100 mA g⁻¹ for two cycles and then cycled at 1,000 mA g⁻¹. The initial discharge capacity of the hollow C is 538 mAh g⁻¹ at 100 mA g⁻¹ with an initial Coulombic efficiency of 59.8%. The reversible capacity at 1,000 mA g⁻¹ is approximately 200 mAh g⁻¹.

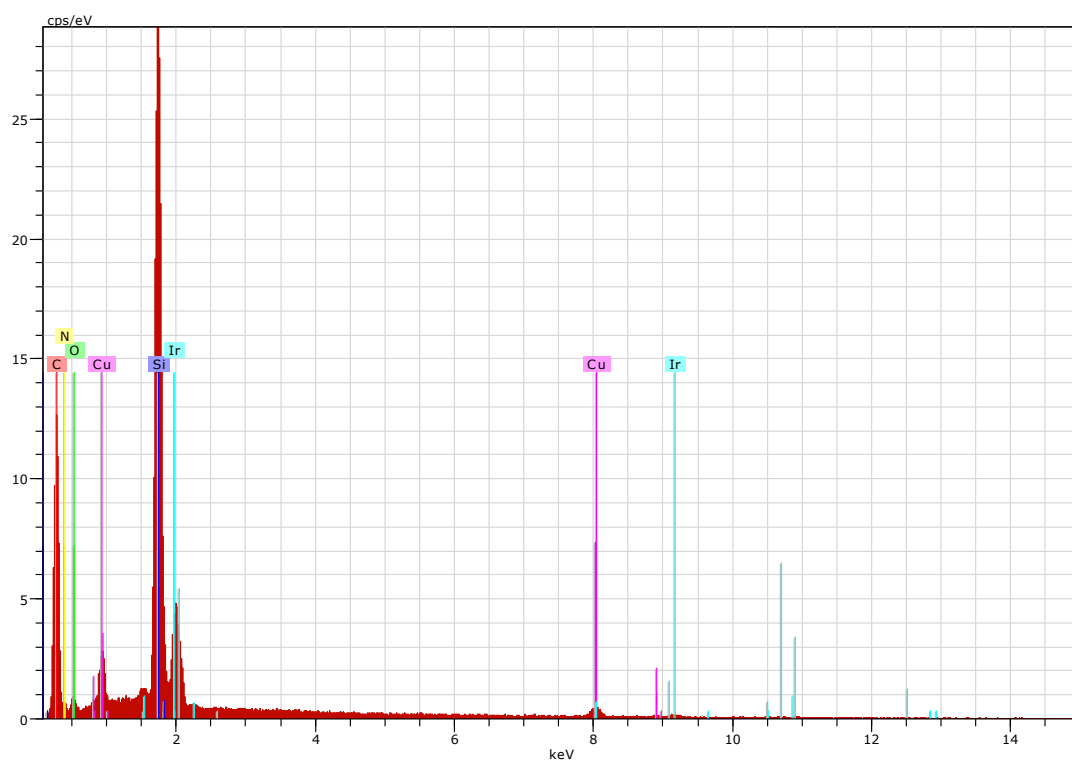


Figure S22. EDS analysis of Si@C@void@C. The results are summarized in Table S4.

Table S4. The EDS analysis results.

El	AN	Series	unn. C [wt.%]	norm. C [wt.%]	Atom. C [at.%]	Error [%]
C	6	K-series	30.13	30.17	47.96	3.7
N	7	K-series	16.80	16.82	22.93	3.4
O	8	K-series	7.54	7.55	9.01	1.5
Si	14	K-series	24.22	24.25	16.49	1.0
Cu	29	K-series	7.45	7.46	2.24	1.1
Ir	77	M-series	13.72	13.74	1.36	0.6
Total:			99.87	100.00	100.00	

The C, N, O, and Si contents in the Si@C@void@C were calculated to be 38.29, 21.35, 9.58, 30.78 w.t %, respectively, by excluding Cu and Ir.

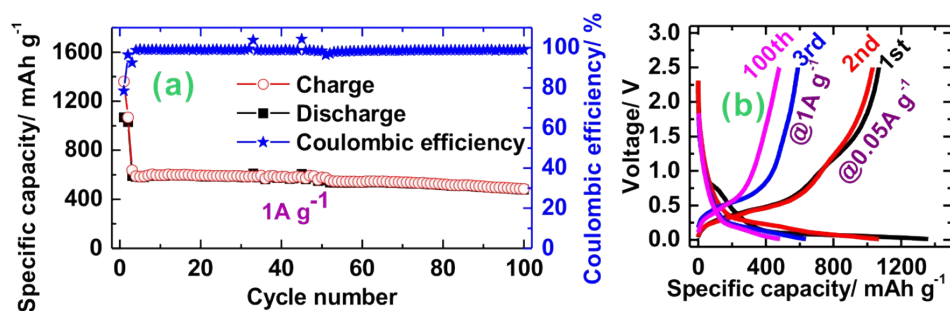


Figure S23. (a) Cyclic performance (b) charge/discharge curves of a Si@void@C with a higher Si content. After activation at 50 mA g⁻¹, the cell was cycled at 1,000 mA g⁻¹, exhibiting a reversible capacity of approximately 590 mAh g⁻¹ and retaining 82% of the capacity (479.2 mAh g⁻¹) after 100 cycles. Note that the voltage upper limit here was extended to 2.5 V, which led to a higher Coulombic efficiency (78.5%). When limiting the voltage limit within 2.0 V, the Coulombic efficiency was 75.1%. The higher Si content in the Si@C@void@C resulted in a higher Coulombic efficiency. The C shells, carbonized from PANi, possess a large specific surface area. The specific surface area of the Si@C@void@C is approximately 226 m² g⁻¹, much higher than that of Si nanoparticles employed here (27 m² g⁻¹).

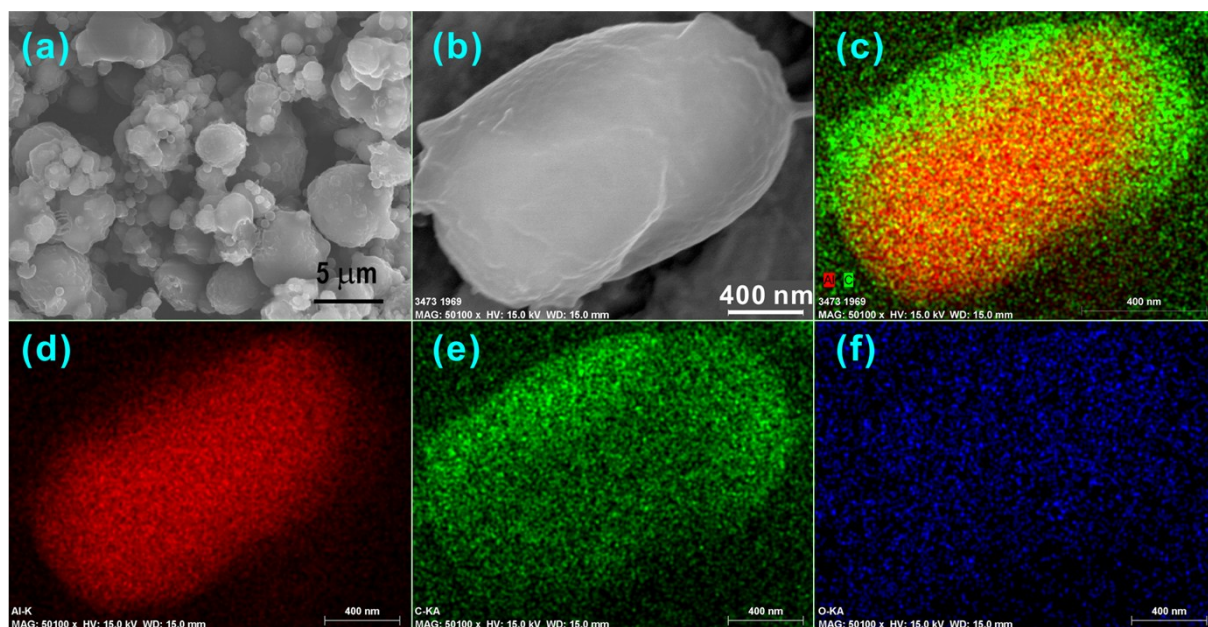


Figure S24. (a,b) SEM images of PS-coated Al and (c-f) EDS elemental mapping for an individual particle shown in (b): (c) blend of Al and C, (d) Al, (e) C, and (f) O. PS was well-coated on the surface of Al particles.

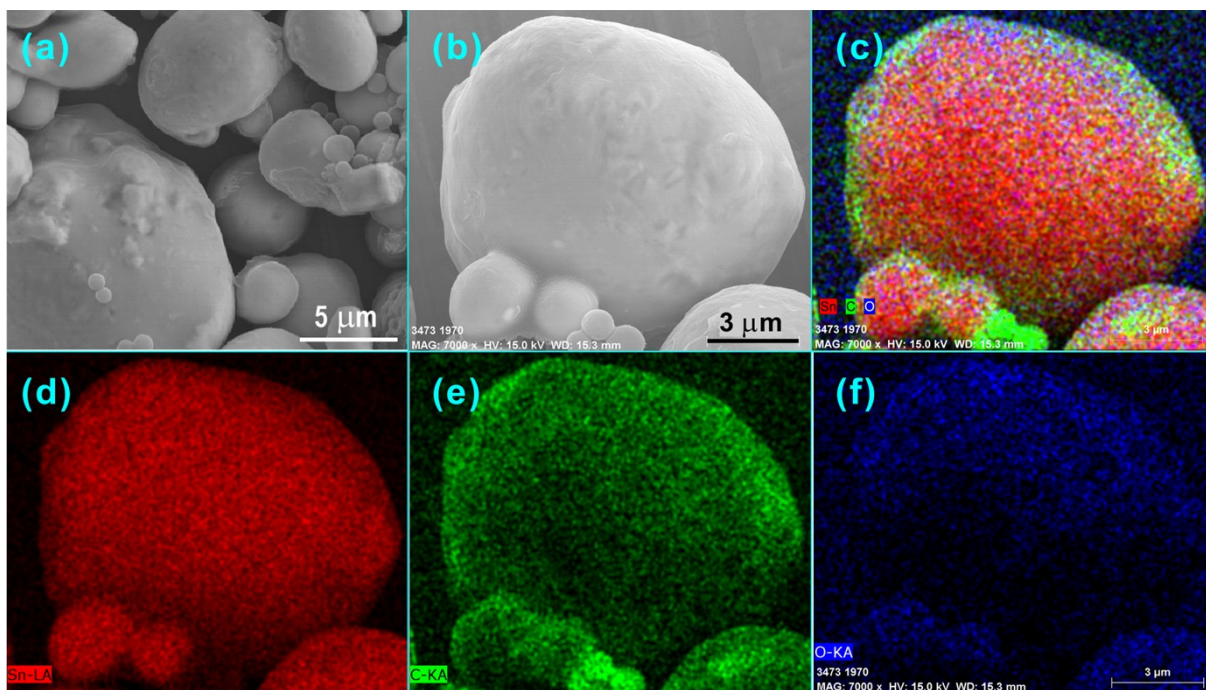


Figure S25. (a,b) SEM images of PS-coated Sn and (c-f) EDS elemental mapping for an individual particle shown in (b): (c) blend of Sn and C, (d) Sn, (e) C, and (f) O. PS-coated Sn was demonstrated using conventional Sn powders (particle size less than 25 μm). It is difficult to coat thick PS on large particles (up to 25 μm); however, the EDS elemental mapping indicates the successful coating C on the Sn particles.